Journal of Digital Imaging (2019) 32:808–815
https://doi.org/10.1007/s10278-018-0162-z

Convolutional Neural Networks for the Detection and Measurement of Cerebral Aneurysms on Magnetic Resonance Angiography

Joseph N. Stember[1] · Peter Chang[2] · Danielle M. Stember[3] · Michael Liu[1] · Jack Grinband[1] · Christopher G. Filippi[4] · Philip Meyers[1] · Sachin Jambawalikar[1]

Published online: 3 December 2018

Abstract

Aneurysm size correlates with rupture risk and is important for treatment planning. User annotation of aneurysm size is slow and tedious, particularly for large data sets. Geometric shortcuts to compute size have been shown to be inaccurate, particularly for nonstandard aneurysm geometries. To develop and train a convolutional neural network (CNN) to detect and measure cerebral aneurysms from magnetic resonance angiography (MRA) automatically and without geometric shortcuts. In step 1, a CNN based on the U-net architecture was trained on 250 MRA maximum intensity projection (MIP) images, then applied to a testing set. In step 2, the trained CNN was applied to a separate set of 14 basilar tip aneurysms for size prediction. Step 1—the CNN successfully identified aneurysms in 85/86 (98.8% of) testing set cases, with a receiver operating characteristic (ROC) area-under-the-curve of 0.87. Step 2—automated basilar tip aneurysm linear size differed from radiologist-traced aneurysm size on average by 2.01 mm, or 30%. The CNN aneurysm area differed from radiologist-derived area on average by 8.1 mm^2 or 27%. CNN correctly predicted the area trend for the set of aneurysms. This approach is to our knowledge the first using CNNs to derive aneurysm size. In particular, we demonstrate the clinically pertinent application of computing maximal aneurysm one-dimensional size and two-dimensional area. We propose that future work can apply this to facilitate pre-treatment planning and possibly identify previously missed aneurysms in retrospective assessment.

Keywords Deep learning · Convolutional neural networks · U-net · Aneurysm · Cerebral aneurysm · MRA

Introduction

Cerebral aneurysms have the potential to cause non-traumatic subarachnoid hemorrhage (SAH), which can result in immediate or delayed morbidity and mortality due to, among other phenomena, vasoconstriction in the post-bleeding state and resulting infarction. Various risk factors for aneurysm rupture have been identified, such as age, gender, and cigarette smoking as well as aneurysm size and location [1–4].

Location is a particularly important predictor of rupture for posterior circulation aneurysms, with those located at the basilar tip having the highest risk of rupture [5]. Basilar tip aneurysms receive the highest location score toward recommendation of treatment on the Unruptured Intracranial Aneurysm Treatment Score (UICATS) [6], since they supply particularly vital territory including the brainstem and basal ganglia. Thus, rupture of a basilar tip aneurysm can be particularly devastating, if not fatal upon presentation. Per UICATS, 4 mm is the size cutoff above which treatment should be considered [6]. As such, accurate detection and size estimation of basilar tip aneurysms is especially clinically important.

However, aneurysms can be missed by radiologists [7, 8]. When found, they are often followed by serial imaging or treated with coils and/or clipping. To help reduce false negative reads and decrease or eliminate inter- and intra-observer variability, automated methods of aneurysm detection have been introduced. These have until recently relied on pre-supplied characteristics or features of the images, such as vessel

✉ Joseph N. Stember
joestember@gmail.com

[1] Radiology, Columbia University Medical Center, 622 West 168th Street, PB 1-301, New York, NY, USA

[2] Radiology, University of California Irvine School of Medicine, Irvine, CA, USA

[3] Neurology, New York University School of Medicine, New York, NY, USA

[4] Radiology, North Shore LIJ Health System, 300 Community Drive, Manhasset, NY, USA

curvature [9, 10], thresholding [11] or a region-growing algorithm [12]. More recently, deep learning via a convolutional neural network (CNN) has been successfully implemented using a patch-based method applied to MIP MRA images [13].

First described by Long et al. [14], fully convolutional neural networks, utilized in medical imaging analysis, result in a dense classification output matrix equivalent in size to the original input image. Here, we utilize a U-Net fully convolutional architecture described by Ronneberger et al. [15] that uses a symmetric contracting and expanding path with skip connections resulting from the correspondingly cropped feature map from the contracting path. CNN algorithms based on this architecture can provide pixel-wise estimations and therefore can be useful for more detailed spatial predictions, such as aneurysm size.

Aneurysm size is a key risk factor for hemorrhage and an important consideration in treatment risk. Automated aneurysm size determination and flagging of aneurysms above a given threshold size can thus be an important application of CNNs and can allow for pre-populating of radiology reports to improve throughput, in addition to providing a remedy for inter-observer variability in size estimations. We have thus sought to automatically detect cerebral aneurysms from MRA images and generate size predictions for the clinically important subclass of basilar tip aneurysms. The present work applies CNNs to two-dimensional (2D) MIP images. Ultimately, in order to be more clinically useful, future work will focus on CNNs to predict aneurysm location and measure volume for full three-dimensional (3D) image volumes.

Methods

A waiver of informed consent was obtained for this retrospective study, which was approved by our medical center's Institutional Review Board.

Step 1: Training and Testing the CNN

For training and testing of our CNN, 336 bright-blood MIP images from MRAs from 302 patients were analyzed. Of these, all but 3 were obtained using a time-of-flight technique, while 3 were obtained with intravenous gadolinium. All images were positive for aneurysm, as determined by the associated finalized radiology report. The 336 images were each single images of a different aneurysm or different aneurysm viewing angle. Some patients had multiple aneurysms that were analyzed, and in a few cases, the same aneurysm was analyzed at a different viewing angle. Aneurysm size lower cutoff was 3 mm, to correspond with the lower limits of diagnostic accuracy using the time-of-flight algorithm with a range of up to 23 mm. Aneurysm location included carotid arteries, proximal portions of the middle cerebral arteries, anterior communicating arteries, vertebral arteries, posterior communicating arteries, basilar artery, and distal branches of the anterior, middle, and posterior cerebral arteries.

Data was collected on 1.5- and 3-T scanners at our institution and obtained from the PACS database as png files using FastStone Capture 9.0 for screen capturing. Resolution was on average 1 mm per pixel. MIPs were obtained from one slice through the entire volume every 10° of rotation about the x and z axes. Angles for image capture were selected so that the aneurysm was in profile. When the appropriate angle was selected, a single image was manually selected around the aneurysm.

Depending on the size of the rectangular region selected by the screen capture, the dimensions of the images varied. However, they were all resized to be 256 × 256 squared pixels. All images were positive for aneurysm. Screen capture rectangular regions were obtained with the aneurysm generally occupying a substantial portion of the two-dimensional field-of-view in order to ensure that the CNN downsampling steps did not erase or significantly diminish the aneurysms in the corresponding network layers. It should be noted that selection of 2D MIP images in this fashion, though convenient for this proof-of-principle study, would not be readily applicable in routine clinical scenarios. Ultimately, a generalization to segmentation of fully 3D image volumes is needed for this utility.

For each thusly selected 256 × 256 squared pixel image, a region-of-interest (ROI) was traced around the aneurysm by a fourth-year radiology resident (JNS) using Matlab R2017a (Mathworks, Natick, MA). This resulted in a binary mask image consisting of ones in the position of the aneurysm and zeros outside.

Of the 336 image files, 250 were selected randomly for training and validation, and the remaining 86 images were reserved for testing. The set of 250 training and validation images was augmented by (1) random vertical and horizontal image flips; (2) random image rotation by 0 to 360°; (3) random affine shear; (4) random displacement by − 10 to + 10 voxels in row and column directions; and (5) random scaling by 75 to 150%. In so doing, an additional 250 images were generated, for a total of 500 images. The image files were normalized to have zero mean and unit standard deviation, in order to reduce network susceptibility to covariate shift. At this point, 80% of the 500 images were assigned randomly for training and the other 20% for validation.

Training was performed using Python 3.7.0 and the packages Tensorflow and Keras on a workstation with three 1080 NVIDIA Ti GPUs (11 Gigabytes each) with two 18-core 2.10 Gigahertz Intel Xeon E5-2695 v4 CPUs and 256 GB system RAM. The aneurysm images were used as input to a 20-layer neural network based on the U-net (Fig. 1), which has been shown to be effective for medical image segmentation [16–18]. Briefly, the U-net is a CNN that consists of

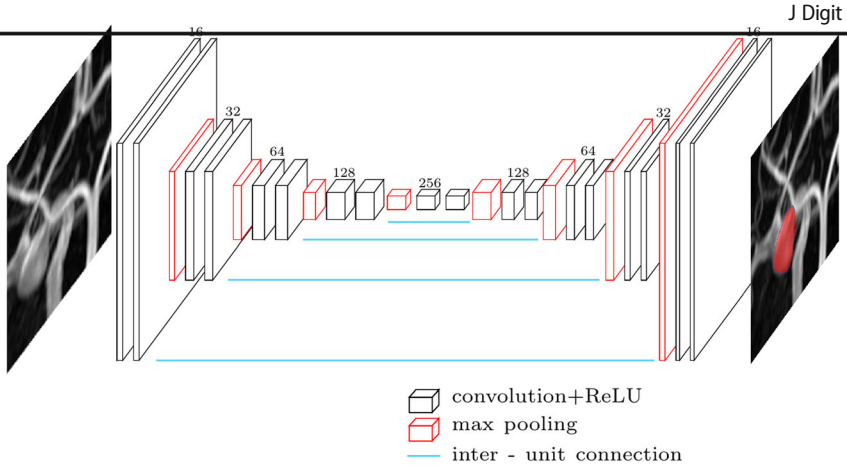

Fig. 1 Illustration of the U-net architecture employed for training of aneurysm MIP images. An example training image is shown on the left, which acts as input that is fed through successive layers of the network in the forward propagation component of training and predicts an aneurysm mask on the right. The numbers above each group of layers in the presented network correspond to the number of channels of the corresponding patch size

contracting and expanding paths as well as a connection path to combine features from the contracting and expanding paths. The contracting path reduces the size of the image feature map as it is passed through successive layers, eschewing pixel-dependent local information for larger scale contextual information. The expanding path up-samples the low resolution information from the contracting path, ultimately re-establishing full pixel resolution of the input image [14, 15].

The training process of CNNs consists of successive iterations of forward followed by backward propagation. The forward propagation involves feeding input images into the network, ultimately returning corresponding output sets of per-pixel likelihood predictions of being within an aneurysm. Comparing this output with the user-annotated mask images yields a loss, calculated here as the negative Dice coefficient D, which measures the overlap between the user-annotated aneurysm mask and the CNN-predicted mask:

$$\text{Loss} = -D = -\frac{2 \times |X \cap Y|}{|X| + |Y|} \tag{1}$$

Backpropagation uses the loss function to update parameter values by the steepest gradient descent method. Given a set of N model weight parameters $\{w_i\}_{i=1}^{N}$, the direction of steepest descent is calculated via

$$-\nabla \mathrm{L} = -\begin{pmatrix} \frac{\partial L}{\partial w_1} \\ \vdots \\ \frac{\partial L}{\partial w_N} \end{pmatrix} \tag{2}$$

The updating process to minimize loss is performed via the Adam optimization algorithm with step length $1 * 10^{-5}$. The model was trained for 60 epochs, after which improvement in accuracy of the prediction and loss values leveled off (Fig. 2). Training time was around 15 min.

Initial weights were randomly selected with a mean of zero according to the default Keras Glorot initialization. This is a standard initialization scheme for CNNs that tunes the variance of the weights to yield activation functions compatible with effective training.

At this point, the 86 test set aneurysm MIPs were run through the trained CNN. Four examples of testing set MIPs with superimposed CNN mask predictions are displayed in Fig. 3, where no size threshold has been applied to those predictions.

A receiver operating characteristic (ROC) curve was calculated by varying size threshold for predicted pixel groups or "clusters" (Fig. 4). For a given threshold value Φ, only predicted aneurysm clusters of size greater than Φ were accepted. The number of true positives consisted of the number of images in the 86 testing set predictions M_{model} for which clusters C_i of size exceeding Φ have a nonzero overlap with the user-annotated aneurysm mask M_{user}. The number of false positives was calculated as the number of predictions with clusters that do not overlap M_{user} (even if one cluster in the image does overlap M_{user}, the presence of a likely smaller predicted region that does not overlap makes this prediction a false positive). The number of false negatives consisted of the number of images for which no aneurysm was predicted, which was simply the total number of predictions, 86, minus the number of true positives. Finally, the number of true negatives was defined by noting that the image space in a given image outside of the aneurysm constitutes an image that lacks an aneurysm. We define this space as that outside of the union of the user-annotated aneurysm mask M_{user} and any predicted aneurysm that overlaps said mask M_{model}, i.e., the complement of the union $(M_{\text{user}} \cup M_{\text{model}})^{\mathrm{C}}$. In order for a prediction to be a true negative, there should be no predicted clusters outside the union, i.e., the following condition should be satisfied:

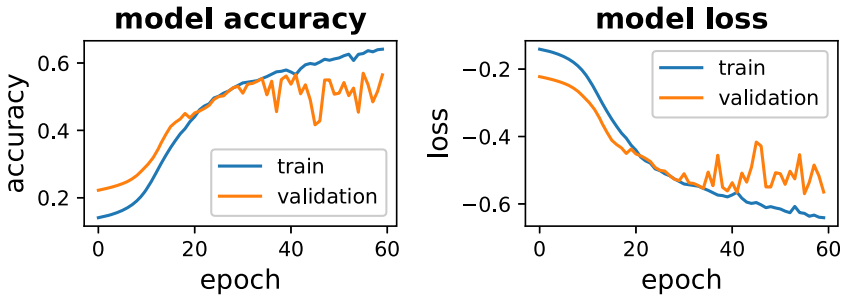

Fig. 2 Training process images for the aneurysm detection CNN. Accuracy (left plot) and loss (right plot) of the training (blue) and validation (orange) sets show improvement with longer training (increasing epochs). Accuracy is calculated as the Dice coefficient and loss is simply negative one times the Dice coefficient

$$\sum_{i=1}^{N_b}\left(C_i \cap (M_{user} \cup M_{model})^{\complement}\right) = 0 \quad (3)$$

where N_b is the total number of predicted clusters in the image.

Step 2: Application to Basilar Tip Aneurysms

With the aforementioned clinical parameters in mind, and having trained our CNN, we subsequently retrieved 14 time-of-flight MRA, basilar tip aneurysms from the PACS database that were distinct from the training and testing set. We imported the corresponding MIP dicom images from the PACS workstation into Matlab, in which the images were cropped in the regions around the aneurysms. All images were resized to 256 × 256 pixels.

At this point, the images were saved as *mat files and imported into Python, in which they were normalized in a similar manner as was done for the training and testing set and then run through the trained CNN. Output prediction masks then underwent a morphological opening before being exported back into Matlab. Small regions of predicted aneurysm of less than 100 pixels were then removed (corresponding to being in a slightly higher specificity/lower sensitivity portion of the ROC curve in Fig. 4), leaving a single largest mask region. Of the 14

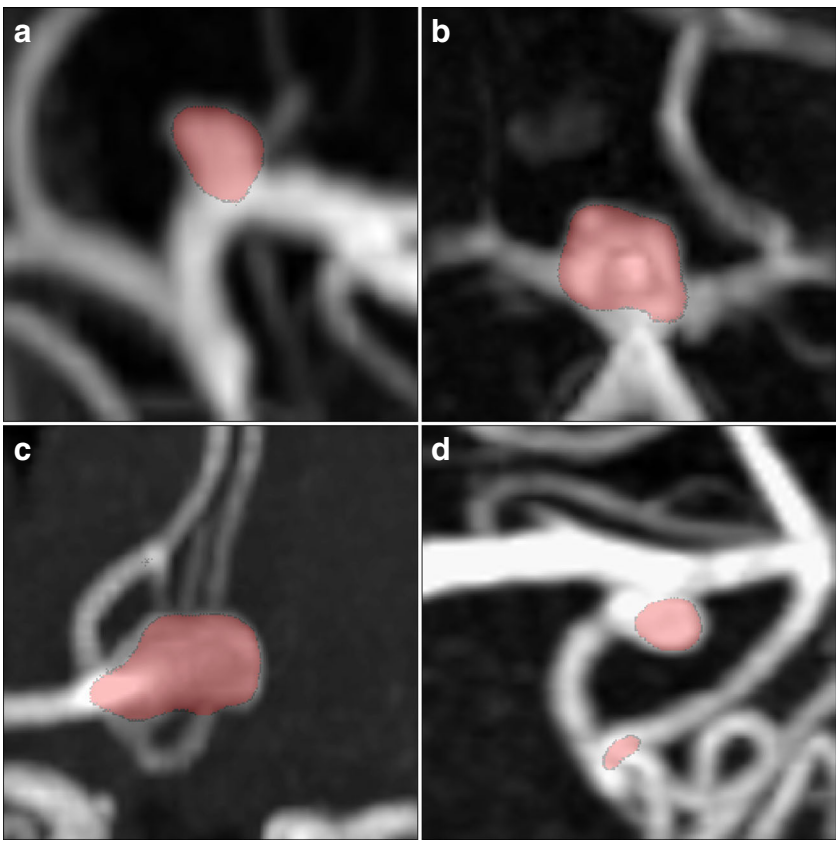

Fig. 3 Panels **a–d** depict four examples of predicted aneurysm masks (red) by the trained CNN overlaid onto the corresponding testing set MRA MIP images. Of note, these predictions are without size thresholding, so that small non-aneurysmal predictions such as the small red region in Fig. 3d

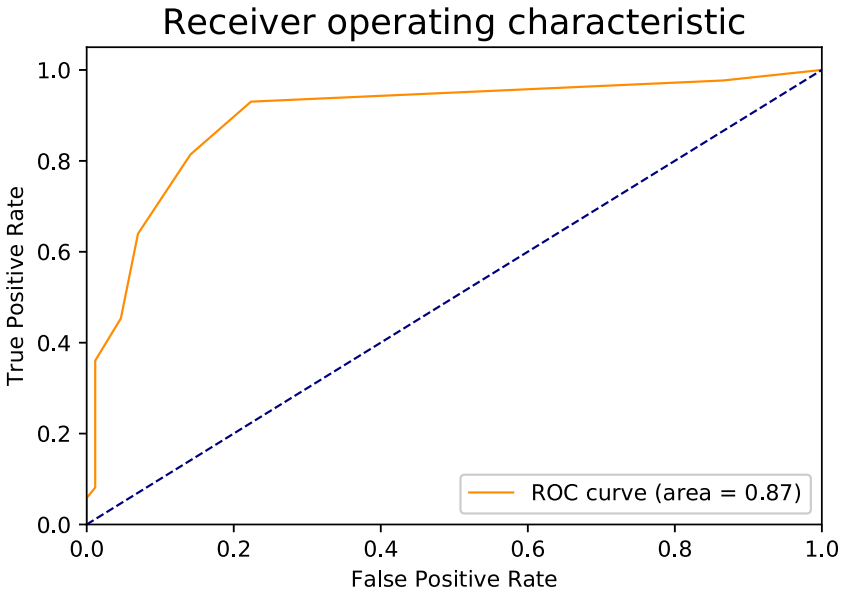

Fig. 4 Receiver operating characteristic curve for the 86 test set images

images analyzed, 13 of them (93%) had nonzero masks overlapping with the aneurysm in the corresponding MIP image.

Surface margins of these 13 predicted aneurysm masks were then calculated in Matlab via the command *bwboundaries*. Then for each aneurysm mask, the set of distances between every possible pair of boundary points $\{x_i, y_i\}$, where i is on the mask boundary b, was calculated and the maximum was taken to be the predicted maximum aneurysm linear size:

$$\text{length}_{\text{CNN}} = \max_{i \in b}\{x_i, y_i\} \quad (4)$$

For comparison, the corresponding MIP images were annotated by JNS (fourth-year radiology resident) for maximum length. Area was calculated simply as the total number of pixels in the aneurysm masks multiplied by the per-pixel resolution in mm^2.

Results

Step 1: Training and Testing the CNN

After training our CNN with the 500 training images, we tested on a set of 86 images. Pixel-wise predictions were rounded to the nearest integer (zero or one), where one indicates overlap with an aneurysm and zero no overlap. Of the 86 predictions with no size thresholding, we achieved nonzero overlap between predicted aneurysm and user-annotated aneurysm in 85 images, for an accuracy of 98.8%. Four examples of the prediction and original MIP images are displayed in Fig. 3. The ROC curve is shown in Fig. 4. The corresponding area-under-the-curve (AUC) was calculated to be 0.87.

Step 2: Application to Basilar Tip Aneurysms

The CNN automated basilar tip aneurysm linear size prediction differed on average from the radiologist-annotated maximum aneurysmal dimension by 2.01 mm or 30%. This difference is noted to be within the interclass size spacing in the UICATS score, so that clinical management would be the same in many cases. An example of CNN-predicted length versus radiologist-annotation is displayed in Fig. 5. The CNN prediction for aneurysm area differed from the radiologist-derived area by an average value of 8.1 mm^2 or 27%. Figure 6 displays how the overall trend of aneurysm size is faithfully replicated by the CNN prediction. The R-value in the best fit line displayed in that figure comparing CNN-predicted area versus user-annotated area is 0.67 with a corresponding p value of 0.01.

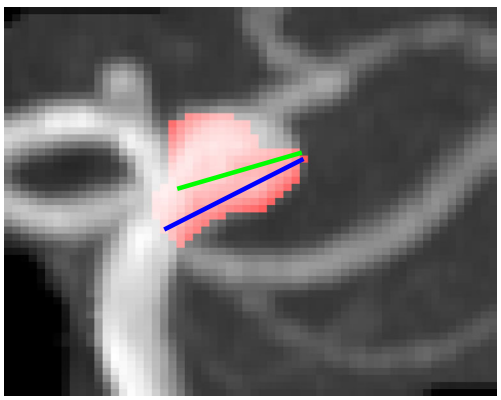

Fig. 5 Example MIP image of a basilar tip aneurysm with user-annotated maximum dimension/size (green line segment). Also overlaid with the MIP is the CNN-predicted aneurysm mask (red) along with the automatically predicted maximum aneurysm based on said mask (blue line segment)

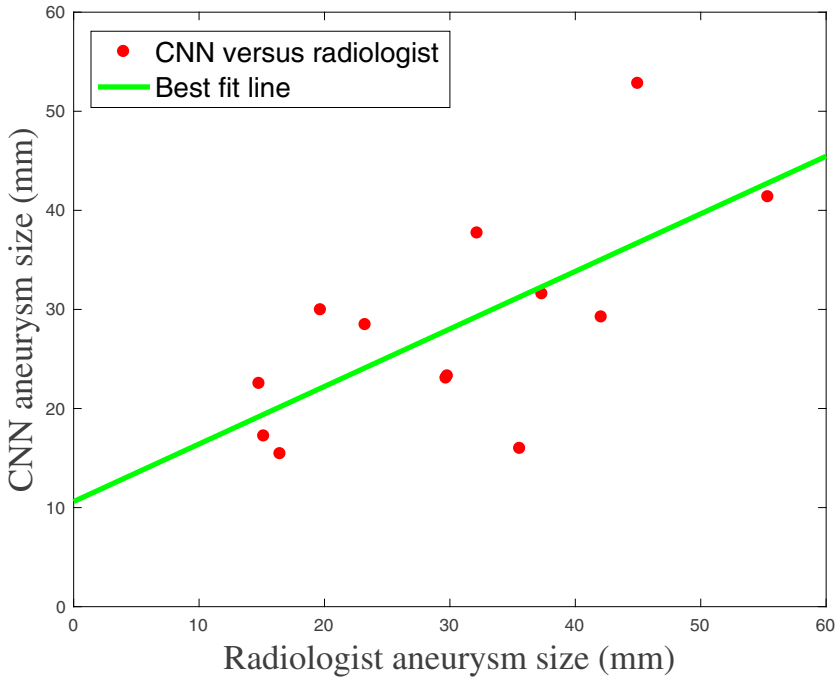

Fig. 6 Comparison of aneurysm area in millimeters between the CNN-based aneurysm area and the corresponding radiologist predictions. The best fit line is displayed in green

Discussion

Though prior work has shown that CNNs can detect cerebral aneurysm presence and location accurately [13], deep learning has not to our knowledge been used to predict aneurysm size. The present work demonstrates that semantic CNNs can derive aneurysm size. Our CNN is particularly well-suited to this task, since it computes aneurysm presence and location on a per-pixel basis with a multi-resolution approach with a U-net-based architecture. Extension to three-dimensional volume predictions is anticipated to be straightforward.

Accurate and fast predictions of aneurysm volume can have a variety of clinical and research applications. Previous work has found that simplified geometric approximations of aneurysm volume are inherently inferior to voxel summation, particularly for irregularly shaped aneurysms [19, 20]. On the other hand, user-performed segmentation for full voxel counting and summation is time-consuming. It would, for example, be unfeasible to measure aneurysm size for data sets numbering in the thousands that could power large studies.

An important clinical application involves coil embolization for aneurysm treatment. "Packing," defined as the ratio of coil volume to aneurysm volume, is an important quantity for aneurysm treatment, whose value depends on volume. Reliable packing value calculations can guide treatments by determining the amount of coil material needed to prevent aneurysm lumen reopening, which can result in rupture [21–24].

Area and volume have both been demonstrated in controlled experiments to be important indicators of aneurysm rupture risk [25, 26]. We propose that in future research, based on extending the current work to 3D CNNs with larger training sets, aneurysm volume could be correlated with incidence of rupture in a large retrospective cohort. This would be feasible with our approach because, as measured above, there is no reliance on inaccurate geometric volume formulas and using trained CNNs avoids time- and labor-consuming manual tracing of aneurysm borders.

Our CNN showed high accuracy and AUC values, even with a relatively small pre-augmentation training/validation set of 250 images. The algorithm was in turn able to predict linear size of the aneurysm to within a small enough margin of user predictions to lie within the UICATS interclass size gradations, and to predict the correct trend in aneurysm area in comparison with radiologist segmentation.

This work builds on prior efforts to detect/predict aneurysms [13] with CNNs by obtaining a per-pixel semantic segmentation and then leveraging this to automatically derive aneurysm size. It is anticipated that CNN mask predictions, and thus size predictions, would become progressively more accurate with larger volumes of training data. It should also be noted that some of the discrepancy between CNN basilar tip aneurysm size predictions and radiologist measurements may be due to undersampling, given the small number of these aneurysms larger than 4 mm that were identified for retrieval.

The higher sensitivity portion of the ROC curve would be particularly useful as a first or second adjunct reader for detection of small aneurysms. This could in practice reduce false negative interpretations and/or help triage unread cases for expedited review. As for any machine learning tool, the reduction in false negatives would in clinical practice need to be balanced against the workflow interference of false positives.

Important limitations to the work presented here include the fact that all images were two-dimensional MIPs. Images were obtained as patches around the aneurysms, so that a relatively large proportion of the image space was taken up by the aneurysms. Normal vessel curvature, such as in the tortuous course of the internal carotid arteries, can hinder two-dimensional MIP images because a normal bend in vasculature may appear from a certain projection as a focal outpouching, i.e., an aneurysm.

As stated above, future work will involve fully three-dimensional MRA and CTA image stacks in order to be more useful clinically and in research. Such an implementation is anticipated to necessitate more training images, since the aneurysms will take up a lesser proportion of the three-dimensional image space and image patches around the aneurysm will be eschewed in favor of the full scanner-derived field of view.

Conclusion

Artificial intelligence implemented as a CNN can predict aneurysm size with some degree of accuracy. Future work will expand the approach to fully three-dimensional data sets and include more training cases for better accuracy. This may enable large-scale automated extractions of aneurysm volumes for research and clinical applications.

Compliance with Ethical Standards

Conflict of Interest The authors declare that they have no conflict of interest.

Publisher's Note Springer Nature remains neutral with regard to jurisdictional claims in published maps and institutional affiliations.

References

1. Backes D, Rinkel GJ, Laban KG, Algra A, Vergouwen MD: Patient- and Aneurysm-Specific Risk Factors for Intracranial Aneurysm Growth: A Systematic Review and Meta-Analysis. *Stroke* **47**:951–957, 2016. https://doi.org/10.1161/STROKEAHA.115.012162
2. Cebral JR, Raschi M: Suggested connections between risk factors of intracranial aneurysms: a review. Ann Biomed Eng 41:1366–1383, 2013. https://doi.org/10.1007/s10439-012-0723-0
3. Brown, Jr RD, Broderick JP: Unruptured intracranial aneurysms: epidemiology, natural history, management options, and familial screening. Lancet Neurol 13:393–404, 2014. https://doi.org/10.1016/S1474-4422(14)70015-8
4. Ghosh S et al.: Association of morphologic and demographic features of intracranial aneurysms with their rupture: a retrospective analysis. Acta Neurochir Suppl 115:275–278, 2013. https://doi.org/10.1007/978-3-7091-1192-5_48
5. International Study of Unruptured Intracranial Aneurysms, I. Unruptured intracranial aneurysms–risk of rupture and risks of surgical intervention. *N Engl J Med* **339**:1725–1733, 1998. https://doi.org/10.1056/NEJM199812103392401
6. Etminan N et al.: The unruptured intracranial aneurysm treatment score: a multidisciplinary consensus. *Neurology* **85**:881–889, 2015. https://doi.org/10.1212/WNL.0000000000001891
7. Elmalem VI, Hudgins PA, Bruce BB, Newman NJ, Biousse V: Underdiagnosis of posterior communicating artery aneurysm in noninvasive brain vascular studies. J Neuroophthalmol 31:103–109, 2011. https://doi.org/10.1097/WNO.0b013e3181f8d985
8. White PM, Wardlaw JM, Lindsay KW, Sloss S, Patel DK, Teasdale EM: The non-invasive detection of intracranial aneurysms: are neuroradiologists any better than other observers? Eur Radiol 13:389–396, 2003. https://doi.org/10.1007/s00330-002-1520-1
9. Raghavan ML, Ma B, Harbaugh RE: Quantified aneurysm shape and rupture risk. J Neurosurg 102:355–362, 2005. https://doi.org/10.3171/jns.2005.102.2.0355
10. Bogunovic H et al.: Automated segmentation of cerebral vasculature with aneurysms in 3DRA and TOF-MRA using geodesic active regions: an evaluation study. Med Phys 38:210–222, 2011. https://doi.org/10.1118/1.3515749
11. Yang X, Blezek DJ, Cheng LTE, Ryan WJ, Kallmes DF, Erickson BJ: Computer-aided detection of intracranial aneurysms in MR angiography. J Digit Imaging 24:86–95, 2011. https://doi.org/10.1007/s10278-009-9254-0
12. Arimura H, Li Q, Korogi Y, Hirai T, Abe H, Yamashita Y, Katsuragawa S, Ikeda R, Doi K: Automated computerized scheme for detection of unruptured intracranial aneurysms in three-dimensional magnetic resonance angiography. Acad Radiol 11:1093–1104, 2004. https://doi.org/10.1016/j.acra.2004.07.011
13. Nakao T, Hanaoka S, Nomura Y, Sato I, Nemoto M, Miki S, Maeda E, Yoshikawa T, Hayashi N, Abe O: Deep neural network-based computer-assisted detection of cerebral aneurysms in MR angiography. *J Magn Reson Imaging*, 2017. https://doi.org/10.1002/jmri.25842
14. Long J, Shelhamer E, Darrell T: Fully convolutional networks for semantic segmentation:3431–3440, 2015. https://doi.org/10.1109/cvpr.2015.7298965
15. Ronneberger, O., Fischer, P. & Brox, T. U-Net: Convolutional Networks for Biomedical Image Segmentation. 9351, 234–241, https://doi.org/10.1007/978-3-319-24574-4_28 (2015).
16. Venhuizen FG et al.: Robust total retina thickness segmentation in optical coherence tomography images using convolutional neural networks. *Biomed Opt Express* **8**:3292–3316, 2017. https://doi.org/10.1364/BOE.8.003292
17. Mohseni Salehi SS, Erdogmus D, Gholipour A: Auto-Context Convolutional Neural Network (Auto-Net) for Brain Extraction in Magnetic Resonance Imaging. *IEEE Trans Med Imaging* **36**:2319–2330, 2017. https://doi.org/10.1109/TMI.2017.2721362
18. Dalmis MU et al.: Using deep learning to segment breast and fibroglandular tissue in MRI volumes. Med Phys 44:533–546, 2017. https://doi.org/10.1002/mp.12079
19. Piotin M, Daghman B, Mounayer C, Spelle L, Moret J: Ellipsoid approximation versus 3D rotational angiography in the volumetric assessment of intracranial aneurysms. AJNR Am J Neuroradiol 27:839–842, 2006
20. Chan SH, Wong KS, Woo YM, Chan KY, Leung KM: Volume measurement of the intracranial aneurysm: a discussion and comparison of the alternatives to manual segmentation. J Cerebrovasc Endovasc Neurosurg 16:358–363, 2014. https://doi.org/10.7461/jcen.2014.16.4.358
21. Sluzewski M, van Rooij WJ, Slob MJ, Bescós JO, Slump CH, Wijnalda D: Relation between aneurysm volume, packing, and compaction in 145 cerebral aneurysms treated with coils.

Radiology 231:653–658, 2004. https://doi.org/10.1148/radiol.2313030460

22. Slob MJ, Sluzewski M, van Rooij WJ: The relation between packing and reopening in coiled intracranial aneurysms: a prospective study. Neuroradiology 47:942–945, 2005. https://doi.org/10.1007/s00234-005-1446-9
23. Kai Y, Hamada J, Morioka M, Yano S, Kuratsu J: Evaluation of the stability of small ruptured aneurysms with a small neck after embolization with Guglielmi detachable coils: correlation between coil packing ratio and coil compaction. *Neurosurgery* **56**:785–792; discussion 785–792, 2005
24. Yasumoto T, Osuga K, Yamamoto H, Ono Y, Masada M, Mikami K, Kanamori D, Nakamura M, Tanaka K, Nakazawa T, Higashihara H, Maeda N, Tomiyama N: Long-term outcomes of coil packing for visceral aneurysms: correlation between packing density and incidence of coil compaction or recanalization. J Vasc Interv Radiol 24:1798–1807, 2013. https://doi.org/10.1016/j.jvir.2013.04.030
25. Austin GM, Schievink W, Williams R: Controlled pressure-volume factors in the enlargement of intracranial aneurysms. Neurosurgery 24:722–730, 1989
26. Valencia A, Morales H, Rivera R, Bravo E, Galvez M: Blood flow dynamics in patient-specific cerebral aneurysm models: the relationship between wall shear stress and aneurysm area index. Med Eng Phys 30:329–340, 2008. https://doi.org/10.1016/j.medengphy.2007.04.011